Cysteine modification can gate non-equilibrium conformational dynamics during enzyme catalysis

Medhanjali DasGupta[1], Dominik Budday[2], Peter Madzelan[1], Javier Seravalli[1], Brandon Hayes[3], Raymond G. Sierra[3,4], Roberto Alonso-Mori[3], Aaron S. Brewster[5], Nicholas K. Sauter[5], Gregory A. Applegate[6], Virendra Tiwari[6], David B. Berkowitz[6], Michael C. Thompson[7], James S. Fraser[7], Michael E. Wall[8], Henry van den Bedem[7,9*], Mark A. Wilson[1*]

* co-corresponding authors: mwilson@unl.edu and vdbedem@stanford.edu

[1]Department of Biochemistry and the Redox Biology Center, University of Nebraska, Lincoln, NE 68588, USA
[2]Chair of Applied Dynamics, University of Erlangen-Nuremberg, D-91058 Erlangen, Germany
[3]Linac Coherent Light Source, SLAC National Accelerator Laboratory, Stanford University, Menlo Park, CA 94025, USA
[4]Stanford PULSE Institute, SLAC National Accelerator Laboratory, Stanford University, Menlo Park, CA 94025, USA
[5]Lawrence Berkeley National Laboratory, Berkeley, CA 94720, USA
[6]Department of Chemistry, University of Nebraska, Lincoln, NE 68588, USA
[7] Department of Bioengineering and Therapeutic Sciences, California Institute for Quantitative Biology, University of California, San Francisco, San Francisco, USA.
[8]Computer, Computational, and Statistical Sciences Division, Los Alamos National Laboratory, Los Alamos, NM 87505, USA.
[9]Bioscience Division, SLAC National Accelerator Laboratory, Stanford University, Menlo Park, CA. USA

Keywords: cysteine modification, radiation-controlled photo-oxidation, radiation damage, serial X-ray crystallography, enzyme conformational dynamics, molecular dynamics simulations

Abstract:
Post-translational modification of cysteine residues can regulate protein function and is essential for catalysis by cysteine-dependent enzymes. Covalent modifications neutralize charge on the reactive cysteine thiolate anion and thus alter the active site electrostatic environment. Although a vast number of enzymes rely on cysteine modification for function, precisely how altered structural and electrostatic states of cysteine affect protein dynamics remains poorly understood. Here we use X-ray crystallography, computer simulations, and enzyme kinetics to characterize how covalent modification of the active site cysteine residue in isocyanide hydratase (ICH) affects the protein conformational ensemble. ICH exhibits a concerted helical displacement upon cysteine modification that is gated by changes in hydrogen bond strength between the cysteine thiolate and the backbone amide of the highly strained residue Ile152. The mobile helix samples alternative conformations in crystals exposed to synchrotron X-ray radiation due to the X-ray-induced formation of a cysteine-sulfenic acid at the catalytic nucleophile (Cys101-SOH). This oxidized cysteine residue resembles the proposed thioimidate intermediate in ICH catalysis. Neither cysteine modification nor helical disorder were observed in X-ray free electron laser (XFEL) diffraction data. Computer simulations confirm cysteine modification-gated helical motion and show how structural changes allosterically propagate through the ICH dimer. Mutations at a Gly residue (Gly150) that modulate helical mobility reduce the ICH catalytic rate and alter its pre-steady state kinetic behavior, establishing that helical mobility is important for ICH catalytic efficiency. Our results suggest that cysteine modification may be a common and likely underreported means for regulating protein conformational dynamics.

Introduction

Enzymes catalyze biochemical reactions by binding, conformationally organizing, and lowering the activation energy barrier of reactants (1). Aside from accelerating certain biochemical reactions, enzymes also inhibit undesired, off-pathway reactions involving highly reactive intermediate species (2). The collective dynamics of enzyme and substrate are often tightly coupled to the catalytic cycle (3-6). For example, substrate binding can shift the enzyme's conformational distribution to structurally and electrostatically re-organize the active site. More controversially, the coupling of conformational dynamics and electrostatics has been proposed to directly contribute to the chemical step of enzyme catalysis, although their precise roles remain actively debated (7-12). Formation of catalytic intermediates transiently modifies the enzyme and may lead to a new protein motion regime that facilitates later steps of catalysis. These motions often span vastly different time-scales, from fs-ns for barrier crossing to ms or longer for product release. While functionally important motions may be present even in a resting enzyme (13), distinguishing functional motions from the many other fluctuations of a macromolecule at equilibrium is challenging (4), leaving major questions about the role of dynamics in catalysis unanswered. For example, how do catalytic intermediates reorganize an enzyme's conformational landscape to facilitate later steps in the catalytic cycle?

For the large class of enzymes that employ a cysteine nucleophile, transient covalent modification of cysteine to form enzyme-bound intermediates is essential for catalysis. These covalent modifications also alter the electrostatic and steric properties of the active site. Cysteine is most reactive in its deprotonated, anionic thiolate form. The negative charge of the thiolate is neutralized upon formation of a covalent bond, thereby transiently removing negative charge from the active site environment during catalysis. Although the chemistry of cysteine reactivity is well-understood (14), protein structural changes promoted by covalently altered cysteines have received less attention. In particular, it is not known how the electrostatic changes resulting from cysteine modification alter non-covalent interaction networks and functionally important protein conformational dynamics in any enzyme.

X-ray crystallography provides an atomically detailed ensemble- and time-averaged view of protein conformational dynamics in the lattice environment (15-18). Technological advances in X-ray sources, detectors, and sample delivery have enabled a new class of crystallography experiments that report on non-equilibrium protein motions in response to external perturbations (19). Because these perturbations can be selected for functional relevance (*e.g.* by the infusion of substrate or induction of a particular modification), the resulting non-equilibrium changes often correspond to functionally important protein motions. In parallel, advances in computer modeling of multiple conformational substates now enable visualizing minor populations of crystalline protein structural ensembles. These approaches have permitted identification of networks of sidechain disorder (20), allowed refinement of whole-protein ensemble models (21), aided identification of minor binding modes of therapeutic ligands (22), and characterized spatial correlations in protein mobility (23).

Isocyanide Hydratase (ICH: EC 4.2.1.103) is a 228-residue homodimeric cysteine-dependent enzyme that hydrates diverse isocyanides to yield N-formamides (24) (Fig. 1A). ICH is a member of the large DJ-1 superfamily and is structurally similar to the homodimeric protein DJ-1. In humans, mutations in DJ-1 (PARK7) cause rare forms of autosomal recessive, early onset parkinsonism (25). The catalytic cysteine in ICH is conserved in most members of the DJ-1 superfamily, where it performs various roles ranging from redox sensing to acting as a catalytic nucleophile in diverse reactions catalyzed by members of this superfamily (26). ICH is one of only two enzymes characterized to date that degrades organic isocyanides, and homologs are

present in many microbes that inhabit soil and water. Some naturally occurring isocyanides are potent antimicrobials (27) and others have recently been shown to be chalkophores, facilitating copper uptake by certain bacteria (28). ICH homologs appear to be important in both of these aspects of isocyanide biochemistry (29-31) as well as for generating biologically active formamides derived from isocyanide precursors (30).

Here, we use X-ray crystallography, molecular dynamics simulation, rigidity theory, mutagenesis, and enzyme kinetics to characterize a set of correlated conformational changes that remodel the ICH active site and propagate across the dimer interface in response to oxidation of the nucleophilic cysteine residue to a cysteine-sulfenic acid. Similar dynamical responses in ICH are expected upon formation of the native thioimidate catalytic intermediate, which resembles cysteine-sulfenic acid. Our analysis of the pre-steady state kinetics of wild-type and mutant ICH suggest that cysteine-gated conformational reorganization may be important for water to access and hydrolyse the catalytic intermediate. The prominence of conformational dynamics in ICH and the tractability of this protein using multiple biophysical techniques make ICH a potent model system for understanding how cysteine modification can modulate functional protein dynamics.

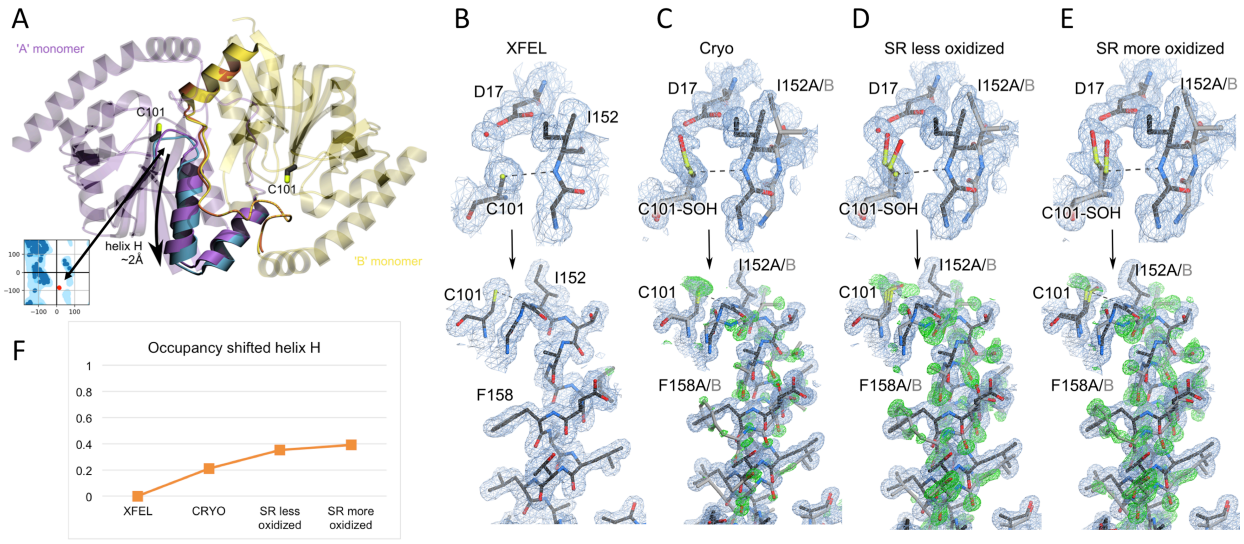

Figure 1: X-ray induced cysteine oxidation drives helical motion in ICH. (A) The ICH dimer is shown as a ribbon diagram, with one protomer colored purple and the other blue. The mobile helix and areas exhibiting correlated backbone-sidechain disorder are rendered darker. Ile152 is a Ramachandran outlier whose backbone torsion angles move with helical displacement. (B-E) The top panels show the environment of Cys101 with varying degrees of oxidation to Cys101-sulfenic acid. $2mF_o$-DF_c electron density is contoured at 0.7 RMSD (blue) and the hydrogen bond between the peptide backbone of Ile152 and Cys101 is shown in a dotted line. "XFEL" is X-ray free electron laser data collected at 298 K, "Cryo" is synchrotron data collected at 100 K (PDB 3NON), "SR less oxidized" is synchrotron data collected at 274 K with an absorbed dose of $2.4x10^4$ Gy, and "SR more oxidized" is synchrotron data collected at 277 K with an absorbed dose of $3.7x10^5$ Gy. The lower panels show the helix in its strained (black) and relaxed, shifted conformations (grey). $2mF_o$-DF_c electron density is contoured at 0.8 RMSD (blue) and omit mF_o-DF_c electron density for the shifted helical conformation is contoured at 3.0 rmsd (green). At 274-277K, increased Cys101 oxidation disrupts the hydrogen bond to Ile152 and results in stronger difference electron density for the shifted helix conformation. (F) The refined occupancy of the helix is plotted versus X-ray dataset, indicating that increases in temperature and Cys101 oxidation result in higher occupancy for the shifted (relaxed) helix conformation.

Results

We previously determined the structure of *Pseudomonas fluorescens* ICH to 1.05 Å resolution using synchrotron X-ray (SR) diffraction data collected at 100 K (29). Weak features in the final difference (mF_o-DF_c) electron density map suggested a collective displacement of an α-helix (helix H; 151–165) proximal to the active site in the wild-type enzyme (Figure 1A). These difference electron density features coincided with a constitutively shifted conformation of this helix observed when the active site nucleophile Cys101 was mutated to alanine (C101A). The C101A mutant eliminates a hydrogen bond between the Cys101 thiolate and the peptide amide of Ile152. Ile152 is a Ramachandran outlier with a severely strained backbone conformation (φ=14°, ψ=-83°) in the wild-type enzyme (Figure 1A) that shifts to a relaxed, unstrained conformation of the displaced helix in C101A ICH (29, 32). In addition, Cys101 was partially oxidized to cysteine-sulfenic acid (Cys-SOH) in the cryocooled crystal structure, presumably due to X-ray photooxidation. However, we were unable to determine how cysteine modification related to helical motion from that cryogenic dataset and thus could not assess the functional significance of these conformational changes.

Cys101 modification triggers conformational changes that remodel the ICH active site

To determine if Cys101 modification directly causes helical displacement in ICH, we collected three X-ray diffraction datasets from wild-type ICH at temperatures ranging from 274-298 K to 1.15-1.6 Å resolution at the Stanford Synchrotron Radiation Lightsource. A serial femtosecond X-ray crystallography (SFX) reference dataset was collected at 298K at the X-ray Pump-Probe instrument (XPP) (33) at the Linac Coherent Light Source (LCLS) X-ray free electron laser (XFEL)(34). Because SFX data are minimally affected by X-ray radiation damage (35), the enzyme suffered no radiation-induced oxidation of Cys101 (Figure 1B). In contrast, the cryogenic dataset collected at 100K (Cryo) shows clear evidence of Cys101-SOH formation (Figure. 1C), as noted previously (29). Two additional ambient temperature datasets were collected using synchrotron radiation (SR). Unlike the XFEL dataset, both SR datasets show oxidation of the catalytic Cys101 nucleophile to a cysteine-sulfenic acid (Cys101-SOH) to varying extents. One dataset shows a minority of oxidized Cys101, with a refined occupancy of 0.23-0.44 for Cys-SOH ("less oxidized", Figure 1D). The less oxidized dataset was collected from a crystal that absorbed a total X-ray dose of 2.2×10^4 Gy (36). The other SR dataset shows complete Cys101 oxidation to Cys-SOH ("more oxidized", Figure 1E) and was collected at a total absorbed X-ray dose of 3.7×10^5 Gy.

The formation of Cys101-SOH causes a large-scale helical displacement near the active site of ICH, altering the microenvironment of Cys101 by opening a pocket near this modified residue. Comparison of the mFo-DFc omit difference electron density around helix H reveals a temperature- and cysteine oxidation-dependent correlated displacement of the helix by ~2 Å (Figure 1B-E). The shifted helical conformation relieves backbone strain at Ile152 at the N-terminus of helix H and simultaneously reorganizes the active site around Cys101. In the damage-free XFEL dataset of the native enzyme with an unmodified Cys101, the helix is exclusively in the strained (*i.e*. unshifted) conformation (Figures 1B, S2). Independent corroborating data were obtained using a lower intensity rotating anode (RA) X-ray source at 298 K, also showing little Cys101 oxidation and one dominant conformation for helix H. Minor difference electron density features are consistent with a small population of the shifted helix in the rotating anode data, but helix H is predominantly in the strained conformation (Figure S1). However, helix H samples a minor shifted population that is correlated with Cys101 oxidation in the cryogenic (100K) SR dataset (Figure 1C). Increasing the temperature of the crystal increases the population of the shifted helix conformation in SR datasets (Fig. 1D,E), presumably because ICH conformational dynamics respond more fully to the Cys101 modification at ambient temperature. Refined occupancies of alternate conformations of helix H confirm a population shift towards the displaced

helix position along this series of data sets that correlates with the extent of Cys101 oxidation (Figure 1F). The shifted helix conformations across data sets are highly similar, suggesting that the observed electron density features are not the result of global radiation damage (37) and that the conformational enrichment results from thermodynamic coupling between this helix and specific, radiation-induced photochemistry at Cys101.

A thiolate-hydrogen bond restraint model for conformational change in ICH

We propose that the radiation-driven oxidation of Cys101 to Cys101-SOH weakens the Cys101-Ile152 H-bond by neutralizing the charge of the Sγ acceptor (Figure 2A,B). We calculated a reduction in the Cys101-Ile152 hydrogen bond energy from -2.2 kcal/mol under reduced conditions (*i.e*. with a thiolate acceptor) to -0.91 kcal/mol upon Cys101-SOH formation [Materials & Methods (38)]. In our model, the weakened hydrogen bond permits the strained backbone conformation at Ile152 to relax and allows helix H to sample the shifted conformation (Figure 2C-E). Together, crystallographic data and physicochemical calculations indicate that cysteine oxidation leads to electrostatic changes that propagate *via* hydrogen bonding and backbone strain to activate helical motion, altering the ICH active site.

The reaction mechanism proposed for ICH has the catalytic Cys101 nucleophile attacking organic isocyanides at the carbenic carbon atom. Proton abstraction from a nearby but unknown general acid leads to a proposed thioimidate intermediate. This thioimidate intermediate, like the radiation-induced oxidation of the Cys101, eliminates the negative charge on Sγ thiolate and will reduce the strength of the hydrogen bond made between the amide H of Ile152 and Cys101 Sγ (Figure 2F). The thioimidate has not been directly observed in ICH, however it is the most plausible intermediate in all candidate ICH mechanisms in which Cys101 is the nucleophile. Therefore, we propose that the C101A mutation, Cys101-SOH, and Cys101-thioimidate intermediate all similarly weaken the interactions that hold helix H in a strained conformation in the resting enzyme.

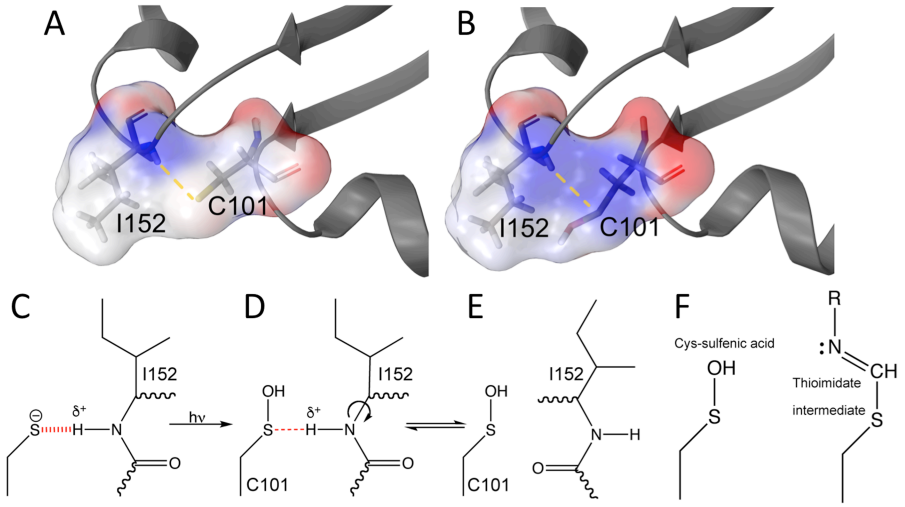

Figure 2: Cys101 oxidation leads to a weakening of the Ile152-Cys101 H-bond. Electrostatic Poisson-Boltzmann surfaces (red negative, blue positive charge) calculated from the Cys101-Ile152 (A) and Cys-SOH-Ile152 (B) environments. Cysteine photooxidation neutralizes the negative charge of the sulfur atom, weakening the N-H … S hydrogen bond. (C-E) Schematic showing covalent modification of Cys101 weakens the hydrogen bond (red dotted/dashed line) to Ile152 and allows relaxation of backbone strain (curved arrow). (F) The catalytic thioimidate covalent intermediate resembles photooxidized Cys101-SOH. Both modifications neutralize negative charge on Cys S_γ.

Molecular dynamics simulations support a thiolate-hydrogen bond restraint mechanism

To test if cysteine modification gates the conformational changes in ICH, we performed molecular dynamics (MD) simulations. We parameterized ICH in the crystal lattice environment using Amber (39) (Methods). Simulations of reduced Cys101 were started from the XFEL crystal structure, with Cys101 in the thiolate state ('XFEL' simulation). For comparison, the oxidized structure was simulated by modifying Cys101 to Cys-sulfenic acid in both protomers in the XFEL structure and removing the catalytic water near Asp17 ('SR' simulation). This starting point is similar to the experimentally determined 'unshifted' cryogenic SR ICH crystal structure (PDB ID 3NON (29)) with Cys101-SOH. While in the crystal structures, and, accordingly, in our simulations, Cys101 were oxidized in both protomers, it is unknown if *in vivo* the ICH dimer performs catalysis synchronously or asynchronously. With Cys101 parameterized in the thiolate form, the Ile152-Cys101 hydrogen bond (Figure 3A) was predominantly maintained in the simulated crystal for the full 1 μs length of the MD trajectory ($d_{avg}(C101_{SG},I152_{H})$ = 2.9Å, Figure 3B). By contrast, simulations of the Cys101-SOH state indicated that the hydrogen bond generally dissociated very early in the trajectory ($d_{avg}(C101_{SG},I152_{H})$ = 4.0Å, Figure 3B).

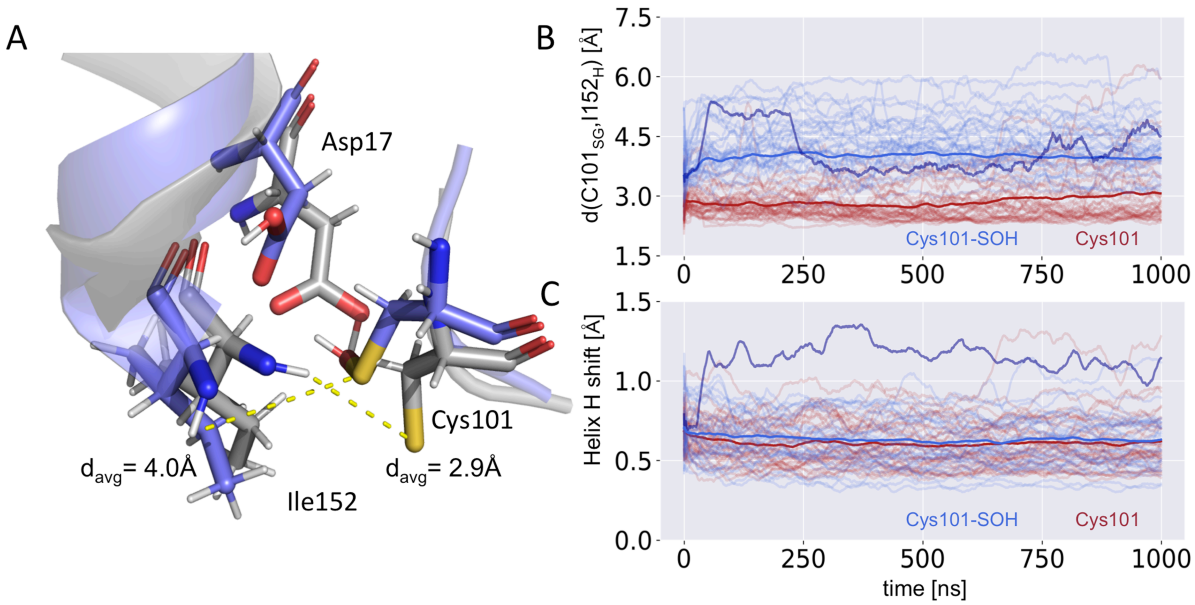

Figure 3: MD simulations support charge-gated conformational changes by cysteine modification. (A) Representative snapshots from ICH crystal MD simulation trajectories, with Cys101 in the thiolate (grey) and in the Cys101-SOH states (slate). The $Cys101_{Sγ}$-Ile152 hydrogen atom distance was markedly shorter on average in simulations with the Cys101 thiolate (2.8 Å) than with the Cys101-SOH (4.3 Å). B) Fluctuations of the $C101_{SG}$-$I152_{H}$ distance in simulations of ICH crystals with Cys101 in the thiolate (red) or Cys101-SOH (blue) state. Each ICH dimer is represented by a transparent line. Opaque red and blue lines denote the average $C101_{SG}$-$I152_{H}$ distance across the dimers. C) Conformational shift of helix H with Cys101 in the thiolate (red) or Cys101-SOH (blue) state. The darker purple lines in panels B and C represent the trajectory selected for Movie S1.

Strikingly, several protomers in the simulated Cys101-SOH crystal experienced a shift of helix H similar to that observed in the ambient temperature synchrotron radiation datasets (mean shift 0.69Å, Figure 3C, movie S1). These helical shifts were observed less frequently in simulations with the Cys101 thiolate (mean shift 0.60Å, Figure 3C), consistent with the hypothesis that local redistribution of cysteine electrostatic charge modulates these long-range motions.

Widespread dynamic conformational responses to radiation-induced cysteine oxidation in ICH

To characterize the extent of the conformational response of the entire ICH dimer to the modification of Cys101, we calculated an isomorphous difference electron density map of the Cys101-S^- rotating anode dataset F_o(RA) and the Cys101-SOH synchrotron radiation dataset F_o(SR) (Materials & Methods) (Figure 4A,B). We phased the map with a structural model obtained from the rotating anode data set. Isomorphous difference maps provide an unbiased view of the difference in molecular conformation between two data sets. The F_o(RA) – F_o(SR) isomorphous difference map reports specifically on changes in ICH that occur in response to oxidation of Cys101. The widely distributed difference features in this electron density map (Figure 4A,B) indicate that ICH responds to Cys101 oxidation with conformational changes across the whole dimer, but with marked heterogeneity in their distribution. We selected the rotating anode dataset as the unmodified reference amplitudes because of greater noise in the XFEL data from the sample injector and experimental geometry introducing errant helium and solvent scatter on a shot-to-shot basis. Nonetheless, a F_o(RA) – F_o(XFEL) map (Figure S3) revealed only minor difference features, suggesting the widespread dynamic response observed in the F_o(RA) – F_o(SR) difference map is due to Cys101 oxidation.

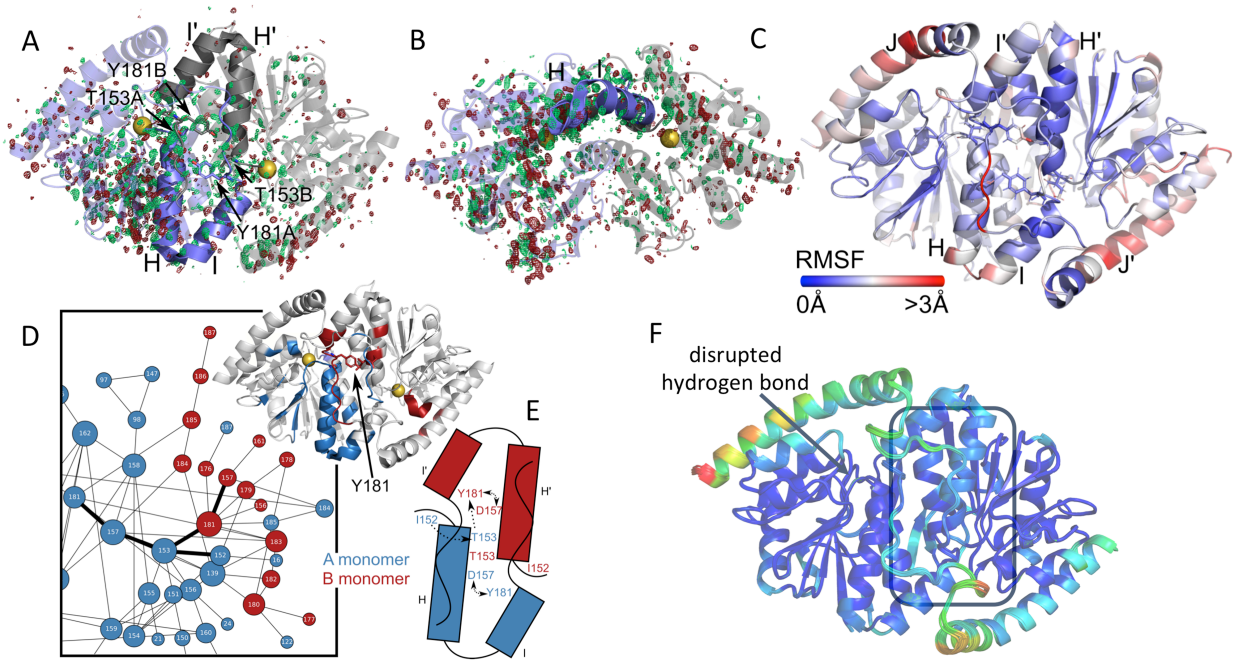

Figure 4: Isomorphous difference map and contact analysis indicate broadly altered structure and dynamics connect active sites. (A,B) An isomorphous difference map calculated between the rotating anode (RA) and 274K synchrotron radiation datasets (F_{oRA} – F_{oRT}) reveals difference features (green, positive; red, negative) distributed throughout the dimer, suggesting broadly altered structure and dynamics upon formation of the cysteine-sulfenic acid in the 274K synchrotron radiation (F_{oRT}) dataset. The 'A' conformer is shown in slate, and the 'B' conformer in grey transparent cartoon representation. Helices H and I are shown opaque in both conformers. The catalytic nucleophile is shown in spheres. (B) is the ICH rotated 90° about the horizontal compared to (A). Difference electron density features are non-uniformly distributed, with stronger features near helix H in the A conformer, and along region B169-B189, which contacts the N-terminal end of helix H. Isomorphous difference features were calculated using an F_o sigma cutoff of 2.0 in both cases and maps were contoured at +/- 3.0 RMSD. (C) Root Mean Square Fluctuations calculated from MD simulations indicate highest fluctuations in linker I-J of the B protomer. Helix H of the A protomer just underneath the linker also shows elevated RMSF. (D) CONTACT analysis identifies allosteric

coupling across the dimer interface, in striking agreement with isomorphous difference maps and RMSF from panel C. The A protomer is color-coded in blue, the B protomer in red. Residues identified in the CONTACT analysis are projected onto the cartoon representation. (E) Schematic of residues allosterically communicating across the dimer interface. (F) Conformational ensemble of motion modes in Kinematic Flexibility Analysis enriched after the $C101_{SG}$-$I152_{H}$ H-bond in the A protomer is disrupted. Consistent with the MD simulations, the IJ linkers in both conformers, which are in contact with helices H, show increased conformational dynamics, especially near both active sites. Motion modes associated with helix J are also enriched.

Unsurprisingly, the F_o(RA) – F_o(SR) difference map features are most prominent in protomer A near the active site and the mobile helix H (Figure 4A). Difference features at the active site correspond to the dramatic conformational change of the diglycyl motif and Ile152, while those near the interface of helix H and the β-sheet in protomer A reflect residues adjusting their position in response to helix H motion. There are far fewer peaks in protomer B, consistent with the absence of mobility of helix H' in that protomer. However, there are significant F_o(RA) – F_o(SR) difference map features along the C-terminus of helix I' in protomer B, which sits at the dimer interface and directly contacts ThrA153 through TyrB181 (Figure 4A,B). These peaks likely report on conformational changes propagating from protomer A through the I'-J' linker (residues 181-185) into protomer B. By contrast, the difference map around the C-terminus of helix I and linker I-J in protomer A (which packs against the stationary helix H of protomer B) is comparatively featureless.

To compare the simulation results to the conformational dynamics observed in the crystal structures, we calculated Root Mean Square Fluctuations (RMSFs) for all residues in a dimer of the Cys101-SOH simulation that experienced a helical shift (Figure 4C, Movie S1). We observed excellent qualitative agreement with the isomorphous difference maps. Interestingly, while the crystal structure revealed similar magnitude of conformational disorder in helix H and linker I'-J', the simulations indicate that the conformational shift in linker I'-J' towards the unshifted helix H' and corresponding active site is much larger than observed in the crystal structure (Figure 4C, Movie S1). Notably, our simulations suggest that the I'-J' conformational shift can precede relaxation of the strained Ile152 conformation and subsequent shift of helix H by several nanoseconds. Together with the asymmetry in the difference map features around linker I-J in both protomers (Figure 4A,B), the MD simulations suggest that the linker plays a functional role in allosterically communicating dynamical changes in protomer A across the dimer interface into protomer B.

Allosteric communication between protomers

We further examined the dynamical communication across the dimer interface in ICH using CONTACT network analysis. CONTACT elucidates pathways of collective amino acid main- and sidechain displacements through mapping van der Waals conflicts that would result from sidechain conformational disorder if correlated motions are not considered (20). CONTACT identified a large network of correlated residues in protomer A (with the mobile helix) that connects with a smaller network in protomer B (Figure 4D, S4), corroborating the isomorphous difference map. The key residues in CONTACT analysis that bridge the dimer interface are Tyr181 and Thr153 (Figure 4E), which are also key residues identified in the isomorphous difference map.

To understand how the active site Cys101-Ile152 hydrogen bond modulates conformational dynamics, we used Kinematic Flexibility Analysis (KFA,(38)). KFA represents a molecule as a kinematic linkage with dihedral degrees of freedom and hydrogen bonds and hydrophobic contacts as constraints. Conventional rigidity analysis (40) of ICH with KFA revealed that changes in protein flexibility between the unshifted and shifted conformations are

concentrated on the IJ linkers (Figure S5). In contrast to traditional molecular rigidity analysis, KFA can provide an explicit basis for orthogonal protein motion modes coupled to energetic penalties incurred by perturbing the constraint network. KFA can rank-order protein motions by the magnitude of free energy changes calculated from non-covalent interactions and molecular rigidity (Supplemental Information). We analyzed how motion modes corresponding to the lowest free energies in the structure without Cys101 modification change when the H-bond is intact in both A and B protomers (C101-I152$_{A\&B}$) to when this H-bond is disrupted in protomer A (C101-I152$_{B}$). These altered motion modes are the ones most affected by disruption of the hydrogen bond. Among the top 100 modes with lowest free energy in each of Cys101-Ile152$_{A\&B}$ and Cys101-Ile152$_{B}$, we identified ten modes that showed least overlap between the Cys101-Ile152$_{A\&B}$ and Cys101-Ile152$_{B}$ (Figure. S6,S7). We then computed root mean square fluctuations (RMSF) resulting from sampling these motion modes (Figure 4F). Interestingly, we observed that the perturbations in the hydrogen bonding network are propagated primarily to the IJ-linkers and helix J, consistent with the MD simulations. Strikingly, the largest RMSFs within the IJ linkers were observed near the active site in the opposite protomer, suggesting that the two sites are in allosteric communication. Identical analyses on the B-protomer hydrogen bond or the XFEL structure yielded similar results. By contrast, ten randomly selected motion modes lead to conformational changes distributed non-specifically throughout the dimer (Figure S8). Considered together, the isomorphous difference electron density map, CONTACT analysis, KFA, and long-time MD simulations all confirm that local changes in hydrogen bonding at Cys101 initiate a cascade of conformational changes that propagate across the entire ICH dimer in an asymmetric manner.

Our results indicate that the conformational changes upon Cys101-Ile152 H-bond modification in the synchrotron structure correspond to later steps in the catalytic cycle, allowing helical motion that facilitates intermediate hydrolysis and product release. At the same time, increased allosteric transmission during these later steps may prime the other protomer for catalysis.

Cysteine modification-gated conformational dynamics increase ICH catalytic efficiency

Both the proposed thioimidate intermediate and Cys101-SOH neutralize Cys101 charge and diminish the strength of the H-bond to Ile152 (Figure 2C-E). Therefore, the correlated displacement of helix H that occurs in response Cys101-SOH formation is also likely to occur during ICH catalysis. To test how helical mobility is related to ICH catalysis, we designed two mutations, G150A and G150T. G150 is part of a highly conserved diglycyl motif that moves ~3Å to accommodate helical motion in ICH. We reasoned that adding steric bulk at this position would modulate the displacement of helix H. This was confirmed in ambient temperature (274-277 K) crystal structures of G150A and G150T ICH at 1.3 Å and 1.1 Å resolution, respectively. In G150A ICH, helix H samples two major conformations, resembling wild-type ICH (Figure 5A). However, both protomers in the G150A ICH dimer show dual conformations for helix H, while only one protomer of wild-type ICH does (Figure S9). By contrast, the G150T structure shows helix H constitutively shifted to its relaxed (i.e. unstrained at Ile152) position (Fig. 5B). Both G150A and G150T have an alternate Cys101 sidechain conformation which conflicts with the unshifted conformation of Ile152 and helix H (Figure 5A,B, asterisk), indicating that the helix must move partially independently of Cys101 oxidation in these mutants. As in wild-type ICH, G150A shows evidence of Cys101-SOH oxidation in the electron density (Figure 5A). In contrast, Cys101 in G150T ICH is not modified by comparable exposure to X-rays (Fig. 5B). The increased propensity of Cys101 to oxidize when it accepts a H-bond from Ile152 suggests that this H-bond, which can only be donated by the strained helical conformation, is important for enhancing Cys101 reactivity.

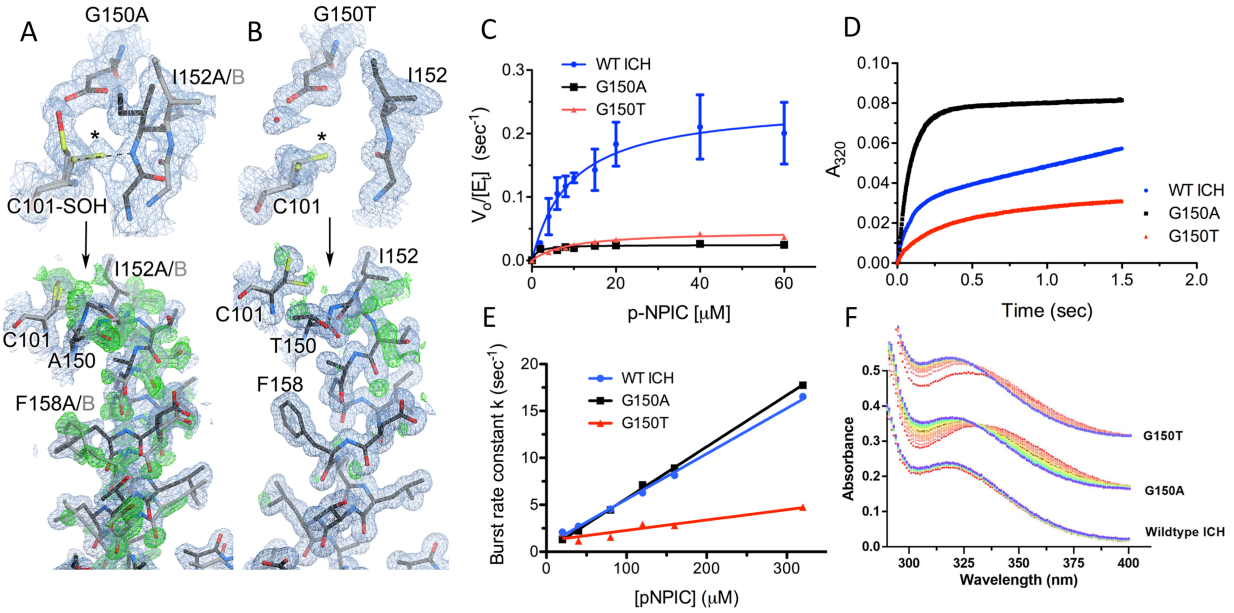

Figure 5: Mutations at Glu150 alter helical mobility and reduce ICH catalytic turnover. (A, B): The top portions show the environment of Cys101 in Gly150A and G150T ICH. $2mF_o$-DF_c electron density is contoured at 0.7 RMSD (blue) and the hydrogen bond between the peptide backbone of Ile152 and Cys101 is shown in a dotted line. Both G150 mutations permit unmodified Cys101 to sample conformations (asterisk) that sterically conflict with Ile152 in the strained helical conformation (black). Therefore, the helix in G150A and G150T ICH must sample shifted conformations (grey) in the absence of Cys101 modification. The lower portions of (A) and (B) show the helix in its strained (black) and relaxed, shifted conformations (grey). $2mF_o$-DF_c electron density is contoured at 0.8 RMSD (blue) and omit mF_o-DF_c electron density for the shifted helical conformation is contoured at +3.0 RMSD (green). The helix samples both strained and shifted conformations in G150A ICH, while the helix is constitutively shifted in G150T. Steady-state (C) and pre-steady state (D, E) enzyme kinetics of wild-type (WT; blue circles), G105A (black squares), and G150T (red triangles) ICH. Both the G150A and G150T mutations result in similar decreases in steady-state k_{cat} compared to WT enzyme. (D) Pre-steady kinetics at 160 uM p-NPIC show a pronounced burst phase for each protein, but with variable burst and steady state rate constants. The divergent pre-steady state profiles indicate that G150A impacts steps after the first chemical step, while G150T affects both early and later steps. (E) The burst rate constant is linearly dependent on substrate concentration, indicative of a second order rate process in the burst phase, consistent with thioimidate formation. WT and G150A have similar second order burst rate constants (slopes), but G150T ICH is lower. (F) Single turnover spectra of ICH enzymes with p-NPIC substrate is shown as a function of time, with time represented from red (early) to blue (later). Spectra were collected every five seconds. At early times, G105A and G150T accumulate a species with λ_{max}=335 nm, likely the thioimidate intermediate that resolves to product in the blue spectra with λ_{max}=320 nm.

Steady-state enzyme kinetics of the G150A and G150T mutants measured using p-nitrophenyl isocyanide (p-NPIC, see Supplemental Information) as the substrate show a ~6–fold reduction in k_{cat} for both mutants compared to wild-type enzyme (Figure 5C, Table 1). In contrast, the K_M values for these mutants are comparable to the wild-type enzyme. Therefore, both G150A and G105T mutants are similarly detrimental to steady-state ICH catalysis. The steady-state kinetics for all proteins were fitted using the Michaelis-Menten model and kinetic parameters are provided in Table 1.

Table 1: Enzyme kinetic parameters

Enzyme	WT	G150A	G150T
Steady State Kinetics			
k_{cat} (sec^{-1})	0.248±0.031	0.025±0.002	0.046±0.003
K_M (μM)	9.262±3.250	1.208 ±0.6134	8.892±1.529
k_{cat}/K_M (M^{-1} sec^{-1})	$2.68x10^4$	$2.07x10^4$	$5.21x10^3$
Stopped Flow mixing			
Burst rate constant (sec^{-1})*	11.395±0.120	11.882±0.071	4.255±0.187
Second order rate constant for burst (M^{-1} sec^{-1})	$4.85x10^4$±943	$5.51x10^4$±557	$1.11x10^4$±999
Steady state rate k_{obs} (sec^{-1})*	0.268±0.001	0.046±0.002	0.095±0.003

*measured at 160 μM p-NPIC
Standard deviations are derived from the fit; data measured n≥3

In contrast to their similar steady-state kinetic behavior, the G150 mutants have divergent the pre-steady state kinetic profiles as measured using stopped-flow mixing. ICH exhibits "burst" kinetics, showing a rapid exponential rise in 320 nm absorbance that then becomes linear as steady-state is reached (Figure 5D). This kinetic burst indicates that the rate-limiting step for ICH catalysis comes after the first chemical step, which is formation of the proposed thioimidate intermediate. The slow step may include resolution of the thioimidate intermediate, product release, or a combination of the two if their intrinsic rates are similar. G150A ICH has a burst exponential rate constant k (~11 s^{-1}) that is comparable to the wild-type enzyme at 160 μM p-NPIC (Figure 5D, Table 1). However, G150T has a reduced burst rate constant of ~4 s^{-1} at the same concentration of substrate, indicating a slower chemical step (Figure 5D, Table 1). This trend is maintained over a 25-350 μM range of p-NPIC concentrations (Figure 5E). A burst rate constant proportional to substrate concentration indicates that the fast chemical step during the burst phase obeys a second order rate law. This is consistent with proposed thioimidate intermediate formation in the burst phase. WT and G150A ICH have very similar second order rate constants (slope of the lines in Figure 5E) for the burst phase, while G150T is markedly slower (Figure 5E, Table 1). Therefore, although both G150A and G150T mutations impair ICH catalysis, the kinetic effect of the G150A mutation is predominantly in steps after formation of the intermediate, while G150T impairs both the rate of intermediate formation and later, rate-limiting steps. Single-turnover UV-visible spectra collected for WT, G150A, and G150T ICH show that G150A ICH accumulates a species whose absorbance maximum is 335 nm, while both WT and G150T accumulate the 320 nm formamide product in the ~30 second deadtime of manual mixing (Figure 5F). In G150A ICH, the 335 nm species slowly converts to the 320 nm product over ~40 s (Fig. 5F), consistent with the slow rate of product formation observed after the burst in G150A pre-steady state kinetics (Figure 5D). We propose that the 335 nm species is the ICH-thioimidate intermediate, and that G150A is impaired in hydrolyzing this covalent intermediate from the active site nucleophile Cys101.

Discussion

Covalent modification is a common and physiologically important perturbation to proteins. Reactive residues such as cysteine are prone to diverse covalent modifications with catalytic or regulatory consequences. In this study, we find that cysteine modification causes changes to H-bonding networks that gate changes in protein dynamics. Oxidation of an active site cysteine thiolate to the sulfenic acid neutralizes its negative charge and weakens a key H-bond, initiating a cascade of conformational changes in ICH that span the entire dimer. Although Cys101-SOH is not a catalytic intermediate, it resembles the proposed Cys101-thioimidate intermediate. Notably, all nucleophilic cysteine thiolates will experience a similar loss of negative charge upon

covalent bond formation. Moreover, because cysteine residues can have multiple roles in a protein, including catalytic nucleophile, metal ligand, acylation target, redox target, and others (41), many different modification-mediated signals may be transduced through altered cysteine electrostatics to impact protein dynamics and function. Therefore, we propose that the cysteine modification is a common and underappreciated means for regulating protein conformational dynamics, expanding the ways in which cysteine can couple protein biophysical properties to cellular needs.

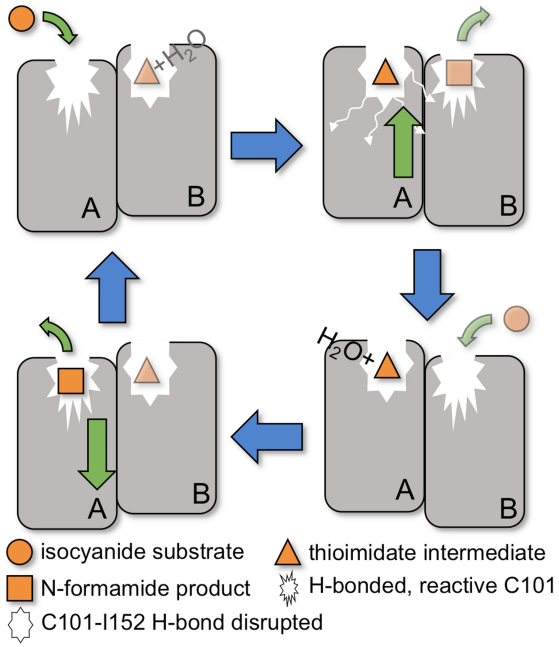

Figure 6: A schematic of the proposed ICH catalytic cycle. Clockwise from upper left: substrate enters the 'A' protomer with the active site Cys101 thiolate poised for nucleophilic attack and the Cys101-Ile152 H-bond intact. Next, formation of the thioimidate intermediate weakens the Cys101-Ile152 H-bond and causes helical motion (green 'up' arrow) that promotes intermediate hydrolysis (indicated by H_2O). Hydrolysis of the thioimidate intermediate restores the reactive C101 thiolate and strengthens the Cys101-Ile152 H-bond, thereby shifting the helix conformational ensemble to favor the strained conformation (green 'down' arrow). The catalytic cycle in the B protomer (transparent) could be in anti-phase to the cycle in the A protomer, although this is speculative.

Cysteine-gated conformational changes in ICH appear to alter the active site environment in order to promote progress along the reaction coordinate. ICH catalyzes a reaction that can be divided into an early phase dominated by nucleophilic attack of Cys101 at the electrophilic carbenoid carbon of its isocyanide substrate and a later phase dominated by hydrolysis of the proposed thioimidate intermediate to release the N-formamide product (Figure S10). The early phase requires a reactive cysteine residue to initiate nucleophilic attack, while the subsequent phase requires water attack at the thioimidate and weaker nucleophilicity of Cys101 (*i.e.* a better leaving group) to release the product. These two phases of ICH catalysis place conflicting demands on the physical properties of Cys101. The divergent pre-steady state kinetics of the G150A and G150T mutants suggest a model where the strained helical conformation of ICH has the highest competence for the initial isocyanide attack by Cys101, forming the thioimidate intermediate. (Figure S10A,B) This is also consistent with the diminished propensity of Cys101 for photooxidation in G150T, where the helix is constitutively shifted, suggesting that Cys101 is less reactive in this environment. After formation of the thioimidate, the helix samples the shifted conformation due to weakening of the Ile152-Cys101 H-bond, dynamically remodeling the ICH

active site (Figures 6 and S10B,C). We propose that the active site samples conformations that favor water attack at the carbon atom of the thioimidate and hydrolysis of the thioimidate intermediate. Upon water attack at the thioimidate to form a tetrahedral intermediate, the H-bond between Cys101 and Ile152 that defines the strained conformation of helix H can reform, thereby stabilizing the nascent Cys101 thiolate and making it a better leaving group. With the strained helical conformation restored, the product is released and leaves the active site poised for another cycle of catalysis (Figures 6 and S10D). The synchrotron X-ray crystallographic data indicate that the G150A mutation enhances sampling of shifted helical conformations even in the absence of Cys101 modification, and this shifted conformation is further populated once the Cys101-Ile152 H-bond is weakened by Cys101-SOH formation. In addition, G150A ICH accumulates a spectrally distinct 335 nm species that we propose corresponds to the thioimidate intermediate. Our interpretation of these data is that the thioimidate intermediate accumulates in G150A ICH owing to an impaired resetting of the strained helical conformation, which reduces the rate of thioimidate hydrolysis and enzyme turnover. Consistent with the pre-steady state kinetic data, this kinetic model for G150A ICH predicts that the early chemical steps promoted by the strained conformation of helix H would not be impaired by the mutation but that the steady-state rate would be significantly diminished. In contrast, the G150T mutation causes a constitutively shifted helix, reducing rates of both initial Cys101 attack at the isocyanide carbon atom in the first chemical step and thioimidate hydrolysis in later steps, as evidenced by the lower burst and steady state rates of G150T ICH. Therefore, the G150A and G150T mutations have divergent effects on the early steps of ICH catalysis but similar detrimental effects on the later, rate-limiting steps.

Modulation of protein dynamics is a powerful way to regulate protein function, as has been characterized in various systems. To our knowledge, ICH is the first example of a non-disulfide cysteine modification regulating functional protein conformational dynamics. Nevertheless, conceptually similar examples of gated conformational dynamical changes exist. Redox-gated changes in flavoprotein structure and dynamics may play a major role in electron transfer by these proteins (42), and similar electron- or charge-coupled gating events occur in diverse systems (43-45). Photoactivatable tags that modulate sampling of active enzyme conformations have been used to create catalytically enhanced enzymes (46). In the DJ-1 superfamily to which ICH belongs, Cys106 oxidation to Cys106-SO_2^- in DJ-1 results in little change in global protein conformation but stabilizes the protein by over 12 °C (47). This stabilization is thought to be due to a strong (2.47 Å) hydrogen bond between Cys106-SO_2^- and Glu18 that forms upon oxidation, reducing protein dynamics and stabilizing the protein.

More generally, transient covalent modification of proteins changes their potential energy surface. Therefore, various covalently modified species of a protein in the cell are likely to be dynamically distinct, providing another mechanism of diversifying protein function. The many potential covalent modifications of cysteine make this residue of particular importance for understanding how cellular signaling states, metabolite pools, and stress conditions couple to functional protein dynamics through the modification of amino acids in proteins. Future work on ICH and other cysteine-containing proteins will illuminate the diverse mechanisms by which cysteine-gated conformational changes can regulate protein function.

Methods

Crystallization, data collection, and processing. *Pseudomonas fluorescens* ICH was expressed in *E. coli* as a thrombin-cleavable, N-terminally 6xHis-tagged protein and purified as previously described (29). All of the final proteins contain the vector-derived amino acids “GSH” at the N-terminus. Wild-type ICH, the G150A, and the G150T mutants were crystallized by hanging drop vapor equilibration by mixing 2 µL of protein at 20 mg/ml and 2 µl of reservoir (23%

PEG 3350, 100mM Tris-HCl, pH 8.6, 200 mM magnesium chloride and 2 mM dithiotheritol (DTT)) and incubating at 22°C. Spontaneous crystals in space group $P2_1$ appear in 24-48 hours and were used to microseed other drops after 24 hours of equilibration. Microseeding was used because two different crystal forms of ICH crystals grow in the same drop and those in space group $P2_1$ are the better-diffracting crystal form. Notably, seeding G150T ICH using wild-type ICH crystals in space group $P2_1$ results exclusively in G150T crystals in space group C2 with one molecule in the asymmetric unit (ASU).

Cryogenic (100K) synchrotron data (PDB 3NON) were previously collected at the Advanced Photon Source beamline 14BM-C from plate-shaped crystals measuring ~500x500x150 µm that were cryoprotected in 30% ethylene glycol, mounted in nylon loops, and cooled by immersion in liquid nitrogen as previously described (29). Ambient temperature (274 K and 277 K) synchrotron data sets were collected at the Stanford Synchrotron Radiation Lightsource from crystals mounted in 0.7 mm diameter, 10 µm wall thickness glass number 50 capillaries (Hampton Research) with a small volume (~5 µl) of the reservoir to maintain vapor equilibrium. Excess liquid was removed from the crystal by wicking, and the capillary was sealed with beeswax. For the 274 K dataset, the crystal was mounted with its shortest dimension roughly parallel to the capillary axis, resulting in the X-ray beam shooting through the longest dimensions of the crystal during rotation. For the 277 K dataset, a large single capillary-mounted crystal was exposed to X-rays and then translated so that multiple fresh volumes of the crystal were irradiated during data collection. This strategy reduces radiation damage by distributing the dose over a larger volume of the crystal. This translation of the sample was factored into the absorbed dose calculation by assuming every fresh volume of the crystal received no prior dose, which is a best-case scenario.

The 100 K and 277 K datasets were collected on ADSC Q4 CCD detectors using the oscillation method. Separate low and high resolution passes were collected with different exposure times and detector distances and merged together in scaling, as the dynamic range of the diffraction data was larger than that of the detector. For the 274 K data, a Pilatus 6M pixel array detector (PAD) was used with shutterless data collection. Because of the very high dynamic range of the detector, a full dataset was collected in a single pass ~5 minutes. The 274 K datasets were indexed and scaled using XDS (48) while the 277K datasets were indexed and scaled and HKL2000 (49). The 100 K dataset was processed as previously described (29).

For the XFEL experiment, large ICH crystals were pulverized by vortexing with a 0.5 mm steel ball, resulting in a suspension of ~50 µm crystal fragments. Samples were delivered to the beam using the microfluidic electrokinetic sample holder (coMESH) injector (50) under atmospheric He pressure conditions at room temperature. The outer line of the coMESH flowed compressed air at 100 psi to protect the charged meniscus from the helium atmosphere. The sample was driven by a syringe pump (KDS Legato 200) at 300 nl/min in its native mother liquor, while being charged between +3 - +5 kV (Stanford Research Systems, SRS PS300) from a charged, wetted stainless steel needle connecting the syringe reservoir to the 100 µm x 360 µm x 1.5 m fused silica capillary. Serial data were collected at LCLS-XPP (SLAC National Accelerator Laboratory) using a Rayonix MX170HS detector, with an FEL X-ray beam focused to below 5 µm at 10Hz. The XFEL diffraction data were processed with cctbx.xfel (51). Of the 28,714 images collected, 1,112 were indexed and their intensities were integrated. Three postrefinement cycles to correct the intensity measurements and merge the data were carried out with PRIME (52) with a Lorentzian partiality model, and using the target unit cell dimensions of SR WT ICH. Final parameters for PRIME included gamma_e = 0.001, frame_accept_min_cc = 0.60, uc_tolerance = 5, sigma_min = 2.5, and partiality_min = 0.2, to obtain the structure factor amplitudes X-ray crystallographic data statistics for all datasets are provided in Table S1.

Model refinement. All refinements were performed in PHENIX1.9 against structure factor intensities using individual anisotropic ADPs and riding hydrogen atoms (53). Weights for the ADP refinement and relative weights for the X-ray and geometry term were optimized. The alternate conformation for helix H (residues 148-173 in chain A) was modeled manually as a single occupancy group, reflecting the presumed correlated displacement of sidechain and backbone atoms. Other disordered regions were also built into multiple conformations manually in COOT (54) if supported by $2mF_o$-DF_c and mF_o-DF_c electron density maps. Occupancies of these groups were refined but constrained to sum to unity in PHENIX. Omit maps were calculated after removing the areas of interest from the model and refining for X cycles. Final models were validated using MolProbity (55) and the validation tools in COOT and PHENIX. Model statistics are provided in Table S2. Isomorphous difference maps were calculated using data to the lowest high resolution of the data sets, 1.45 Å for $F_{oRA} - F_{oRT}$ and 1.6 Å for $F_{oRA} - F_{oXFEL}$.

Special care was taken to avoid model bias in the XFEL structure, which has been reported to be a potential concern for sparse data generated by some serial femtosecond crystallography experiments (56). In addition to refining a model with the single conformation for helix H (Figure 1B), a dual conformation model for this helix was also refined against the XFEL data. Unlike the SR refinements, the dual conformation model for helix H shows no supporting electron density in the $2mF_o$-DF_c maps, confirming that the single helix model is superior for the XFEL data and model bias does not dominate the apparent agreement between model and electron density map in this system (Figure S2)

Molecular Dynamics Simulations. ICH crystals were parameterized using Amber (39). A simulation cell with unit cell dimensions and $P2_1$ symmetry of the crystal structure was created and replicated to obtain a 2x2x2 supercell containing 16 ICH dimers to minimize boundary artifacts in the simulations. 200 mM $MgCl_2$ and 100mM Tris-HCl were added to the simulation cell. While the crystallization conditions also included PEG3350 and DTT, those were omitted from the simulation owing to the large size of PEG and the low concentration (2mM) of DTT. The system was electrostatically neutralized by adding Na^+ ions. SPC/E waters were added to obtain a pressure of approximately 1bar. Simulations of 'XFEL conditions' were started from the XFEL crystal structure, with C101 in the thiolate state. By contrast, the synchrotron structure was simulated by modifying C101 to Cys-sulfenate (Cys-SOH) in the XFEL structure and removing the catalytic water near Asp17. Partial charges for Cys-SOH were determined with HF/6-31G* basis set and the AM1-BCC method in Antechamber (57). The systems were minimized with steepest descent and conjugate gradient algorithms by gradually reducing constraints on the protein atoms. The time step was set to 1 fs for the initial phase of equilibration. Production runs of 1 μs ICH crystal NVT ensembles were carried out with openMM (58) on NVIDIA K80 and P100 GPUs, with an integration timestep of 2 fs, and non-bonded cutoffs of 1 nm. In total, we obtained 4 μs of simulation time for ICH.

The distance of the $I152_H$-$C101_{SG}$ hydrogen bond was calculated for each protomer at time intervals of 500 ps over the course of the simulations. The average $I152_H$-$C101_{SG}$ distance was obtained by averaging over the protomers (bold line, Figure 3B), and then averaging over time. The shifts of helix H were calculated at time intervals of 500 ps by first aligning each protomer to the first frame using all backbone (heavy) atoms giving an $RMSD_{REF}$, and then calculating the backbone (heavy) atom RMSD to the first frame over residues 152 to 166 giving $RMSD_{HELIX}$. We then reported the fraction $RMSD_{HELIX}$/ $RMSD_{REF}$. While RSMD strongly depends on the length of the fragment and flexible loops, generally $RMSD_{HELIX}$/ $RMSD_{REF} > 1$ indicates that the helix shifts more than the rest of the protomer. The average shift was obtained by averaging over the protomers (bold line, Figure 3C), and then averaging over time.

Synthesis of para-nitrophenyl isocyanide (p-NPIC). ICH will accept diverse isocyanide substrates (24). Due to its strong absorption in the visible range ($\lambda_{max=}$320 nm), para-nitrophenyl isocyanide (p-NPIC) was used here. The p-NPIC substrate is not commercially available and was synthesized and characterized using ^{1}H NMR, ^{13}C NMR, IR, mass spectrometry as described in the Supplemental Information (Figures S11-S18).

ICH enzyme kinetics. For the steady state ICH rate measurements, reactions were initiated by the addition of ICH (final concentration of 1 μM) to freshly prepared p-NPIC solutions ranging from 0-60 μM in reaction buffer (100 mM KPO_4, 50 mM KCl, and 20% DMSO). p-NPIC was diluted from a 0.5 M stock solution in dimethyl sulfoxide (DMSO), which was stored at -80 °C and protected from light when not in use. A 200 μl reaction was maintained at 25 °C in a Peltier-thermostatted cuvette holder. The formation of the product, para-nitrophenyl formamide (p-NPF) was monitored at its absorption maximum of 320 nm for two minutes using a UV-Vis Cary 50 Spectrophotometer (Varian, Palo Alto, CA). A linear increase in A_{320} was verified and used to calculate initial velocities. Isocyanides can spontaneously hydrolyse slowly in aqueous solutions, with the rate increasing as pH is lowered. To ensure that all measured product formation was due to ICH catalysis, the rate of spontaneous p-NPIC hydrolysis was measured without added ICH. These values were near the noise level of the spectrophotometer and were subtracted from the raw rate measurements before fitting the Michaelis-Menten model. The extinction coefficient at 320 nm for p-NPF was determined by using ICH to convert known concentrations of p-NPIC to p-NPF, followed by measuring the absorbance at 320 nm. The slope of the resulting standard curve was defined as the extinction coefficient of p-NPF at 320 nm; ε_{320}=1.33x10^{4} M^{-1} cm^{-1}. This p-NPF ε_{320} value was used to convert the measured rates from A_{320}/sec to [p-NPF]/sec. All data were measured in triplicate or greater and mean values and standard deviations were plotted and fitted using the Michaelis-Menten model as implemented in Prism (GraphPad Software, San Diego, CA). Reported K_m and k_{cat} values and their associated errors are given in Table 1.

Pre-steady state ICH kinetics were measured at 25 ˚C using a Hi-Tech KinetAsyst stopped flow device (TgK Scientific, Bradford-on-Avon, United Kingdom). Data were collected for each sample for 2 seconds (instrument deadtime is 20 ms) in triplicate. The final enzyme concentration after mixing was 10 μM and final p-NPIC concentrations were 20, 40, 80, 120, 160, and 320 μM. Product evolution was monitored at 320 nm using a photodiode array detector. Kinetic Studio software (TgK Scientific, United Kingdom) was used to analyze the kinetic data and to fit a mixed model containing a single exponential burst with a linear steady state component: -Aexp(-kt) + mt + C. In this equation, t is time, k is the burst phase rate constant, m is the linear phase (steady-state) rate, A is the amplitude of the burst component, and C is a baseline offset constant. The linear slope m was used to calculate steady state turnover numbers, which agree well with k_{obs} values obtained from steady state kinetic measurements at comparable substrate concentrations. Single turnover experiments were also performed using final concentrations of 40 μM enzyme and 20 μM p-NPIC after manual mixing. Spectra were collected using a Cary 50 spectrophotometer (Varian, Palo Alto, CA, USA). Spectra were collected every 10 seconds with a deadtime of ~5 seconds after manual addition of enzyme.

Structure factor data and refined coordinates are available in the Protein Data Bank with the following accession codes: 6NI4, 6NI5, 6NI6, 6NI7, 6NI8, 6NI9, 6NJA, and 6NPQ.

Acknowledgements
We thank Dr. Donald Becker (University of Nebraska) and Dr. Joseph Barycki (North Carolina State University) and Lauren Barbee (University of Nebraska) for

assistance with ICH kinetic data and analysis. RGS acknowledges the support of the OBES through the AMOS program within the CSGB and of the DOE through the SLAC Laboratory Directed Research and Development Program. ASB and NKS were supported by NIH grant GM117126 to NKS for data-processing methods. MCT and JSF were supported by NSF (STC-1231306), by a Ruth L. Kirschstein National Research Service Award (F32 HL129989) to MCT, and by awards to JSF from NIH (GM123159, GM124149), the David and Lucile Packard Foundation (Packard Fellowship), and the UC Office of the President Laboratory Fees Research Program (LFR-17-476732. HvdB was supported by NIH GM123159. Portions of this work were supported by Nebraska Tobacco Settlement Biomedical Research Development Fund (MAW). Use of the Stanford Synchrotron Radiation Lightsource, SLAC National Accelerator Laboratory, is supported by the U.S. Department of Energy, Office of Science, Office of Basic Energy Sciences under Contract No. DE-AC02-76SF00515. The SSRL Structural Molecular Biology Program is supported by the DOE Office of Biological and Environmental Research, and by the National Institutes of Health, National Institute of General Medical Sciences (including P41GM103393). Use of the Linac Coherent Light Source (LCLS), SLAC National Accelerator Laboratory, is supported by the U.S. Department of Energy, Office of Science, Office of Basic Energy Sciences under Contract No. DE-AC02-76SF00515. This research used resources of the Advanced Photon Source, a U.S. Department of Energy (DOE) Office of Science User Facility operated for the DOE Office of Science by Argonne National Laboratory under Contract No. DE-AC02-06CH11357. Use of BioCARS was also supported by the National Institute of General Medical Sciences of the National Institutes of Health under grant number R24GM111072. The contents of this publication are solely the responsibility of the authors and do not necessarily represent the official views of NIGMS or NIH.

References

1. Ringe D & Petsko GA (2008) Biochemistry. How enzymes work. *Science* 320(5882):1428-1429.
2. Vogeli B & Erb TJ (2018) 'Negative' and 'positive catalysis': complementary principles that shape the catalytic landscape of enzymes. *Curr Opin Chem Biol* 47:94-100.
3. Boehr DD, D'Amico RN, & O'Rourke KF (2018) Engineered control of enzyme structural dynamics and function. *Protein Sci* 27(4):825-838.
4. Henzler-Wildman KA*, et al.* (2007) Intrinsic motions along an enzymatic reaction trajectory. *Nature* 450(7171):838-844.
5. Aviram HY*, et al.* (2018) Direct observation of ultrafast large-scale dynamics of an enzyme under turnover conditions. *Proceedings of the National Academy of Sciences of the United States of America* 115(13):3243-3248.
6. Kim TH*, et al.* (2017) The role of dimer asymmetry and protomer dynamics in enzyme catalysis. *Science* 355(6322).
7. Hay S & Scrutton NS (2012) Good vibrations in enzyme-catalysed reactions. *Nat Chem* 4(3):161-168.
8. Fried SD & Boxer SG (2017) Electric Fields and Enzyme Catalysis. *Annu Rev Biochem* 86:387-415.
9. Kamerlin SC & Warshel A (2010) At the dawn of the 21st century: Is dynamics the missing link for understanding enzyme catalysis? *Proteins* 78(6):1339-1375.
10. Warshel A & Bora RP (2016) Perspective: Defining and quantifying the role of dynamics in enzyme catalysis. *J Chem Phys* 144(18):180901.

11. Glowacki DR, Harvey JN, & Mulholland AJ (2012) Taking Ockham's razor to enzyme dynamics and catalysis. *Nat Chem* 4(3):169-176.
12. Hanoian P, Liu CT, Hammes-Schiffer S, & Benkovic S (2015) Perspectives on electrostatics and conformational motions in enzyme catalysis. *Accounts of chemical research* 48(2):482-489.
13. Weikl TR & Paul F (2014) Conformational selection in protein binding and function. *Protein Sci* 23(11):1508-1518.
14. Poole LB (2015) The basics of thiols and cysteines in redox biology and chemistry. *Free Radic Biol Med* 80:148-157.
15. Furnham N, Blundell TL, DePristo MA, & Terwilliger TC (2006) Is one solution good enough? *Nat Struct Mol Biol* 13(3):184-185; discussion 185.
16. Fraser JS*, et al.* (2011) Accessing protein conformational ensembles using room-temperature X-ray crystallography. *Proceedings of the National Academy of Sciences of the United States of America* 108(39):16247-16252.
17. Smith JL, Hendrickson WA, Honzatko RB, & Sheriff S (1986) Structural heterogeneity in protein crystals. *Biochemistry* 25(18):5018-5027.
18. Wilson MA & Brunger AT (2000) The 1.0 A crystal structure of Ca(2+)-bound calmodulin: an analysis of disorder and implications for functionally relevant plasticity. *Journal of molecular biology* 301(5):1237-1256.
19. Martin-Garcia JM, Conrad CE, Coe J, Roy-Chowdhury S, & Fromme P (2016) Serial femtosecond crystallography: A revolution in structural biology. *Arch Biochem Biophys* 602:32-47.
20. van den Bedem H, Bhabha G, Yang K, Wright PE, & Fraser JS (2013) Automated identification of functional dynamic contact networks from X-ray crystallography. *Nature methods* 10(9):896-902.
21. Burnley BT, Afonine PV, Adams PD, & Gros P (2012) Modelling dynamics in protein crystal structures by ensemble refinement. *eLife* 1:e00311.
22. van Zundert GCPH, Hudson BM, Keedy DA, Fonseca R, Heliou A, Suresh P, Borrelli K, Day T, Fraser JS, & van den Bedem H (2018) qFit-ligand reveals widespread conformational heterogeneity of drug-like molecules in X-ray electron density maps. *J. Med. Chem.* 61(24):11183–11198.
23. Wall ME, Wolff AM, & Fraser JS (2018) Bringing diffuse X-ray scattering into focus. *Curr Opin Struct Biol* 50:109-116.
24. Goda M, Hashimoto Y, Shimizu S, & Kobayashi M (2001) Discovery of a novel enzyme, isonitrile hydratase, involved in nitrogen-carbon triple bond cleavage. *J Biol Chem* 276(26):23480-23485.
25. Bonifati V*, et al.* (2003) Mutations in the DJ-1 gene associated with autosomal recessive early-onset parkinsonism. *Science* 299(5604):256-259.
26. Smith N & Wilson MA (2017) Structural Biology of the DJ-1 Superfamily. *Adv Exp Med Biol* 1037:5-24.
27. Edenborough MS & Herbert RB (1988) Naturally occurring isocyanides. *Nat Prod Rep* 5(3):229-245.

28. Wang L*, et al.* (2017) Diisonitrile Natural Product SF2768 Functions As a Chalkophore That Mediates Copper Acquisition in Streptomyces thioluteus. *Acs Chem Biol* 12(12):3067-3075.
29. Lakshminarasimhan M, Madzelan P, Nan R, Milkovic NM, & Wilson MA (2010) Evolution of new enzymatic function by structural modulation of cysteine reactivity in Pseudomonas fluorescens isocyanide hydratase. *J Biol Chem* 285(38):29651-29661.
30. Lim FY*, et al.* (2018) Fungal Isocyanide Synthases and Xanthocillin Biosynthesis in Aspergillus fumigatus. *MBio* 9(3).
31. Zhu M*, et al.* (2018) Tandem Hydration of Diisonitriles Triggered by Isonitrile Hydratase in Streptomyces thioluteus. *Org Lett* 20(12):3562-3565.
32. Brereton AE & Karplus PA (2015) Native proteins trap high-energy transit conformations. *Sci Adv* 1(9):e1501188.
33. Chollet M*, et al.* (2015) The X-ray Pump-Probe instrument at the Linac Coherent Light Source. *Journal of Synchrotron Radiation* 22:503-507.
34. Boutet S*, et al.* (2012) High-resolution protein structure determination by serial femtosecond crystallography. *Science* 337(6092):362-364.
35. Chapman HN, Caleman C, & Timneanu N (2014) Diffraction before destruction. *Philos Trans R Soc Lond B Biol Sci* 369(1647):20130313.
36. Zeldin OB, Brockhauser S, Bremridge J, Holton JM, & Garman EF (2013) Predicting the X-ray lifetime of protein crystals. *Proceedings of the National Academy of Sciences of the United States of America* 110(51):20551-20556.
37. Russi S*, et al.* (2017) Conformational variation of proteins at room temperature is not dominated by radiation damage. *J Synchrotron Radiat* 24(Pt 1):73-82.
38. Budday D, Leyendecker S, & van den Bedem H (2018) Kinematic Flexibility Analysis: Hydrogen Bonding Patterns Impart a Spatial Hierarchy of Protein Motion. *J Chem Inf Model* 58(10):2108-2122.
39. Case DA*, et al.* (2005) The Amber biomolecular simulation programs. *J Comput Chem* 26(16):1668-1688.
40. Budday D, Leyendecker S, & van den Bedem H (2015) Geometric analysis characterizes molecular rigidity in generic and non-generic protein configurations. *J Mech Phys Solids* 83:36-47.
41. Pace NJ & Weerapana E (2013) Diverse functional roles of reactive cysteines. *Acs Chem Biol* 8(2):283-296.
42. Toogood HS, Leys D, & Scrutton NS (2007) Dynamics driving function: new insights from electron transferring flavoproteins and partner complexes. *FEBS J* 274(21):5481-5504.
43. Danyal K, Mayweather D, Dean DR, Seefeldt LC, & Hoffman BM (2010) Conformational gating of electron transfer from the nitrogenase Fe protein to MoFe protein. *J Am Chem Soc* 132(20):6894-6895.
44. Catterall WA, Wisedchaisri G, & Zheng N (2017) The chemical basis for electrical signaling. *Nat Chem Biol* 13(5):455-463.
45. Liu Y*, et al.* (2017) A pH-gated conformational switch regulates the phosphatase activity of bifunctional HisKA-family histidine kinases. *Nat Commun* 8(1):2104.

46. Agarwal PK, Schultz C, Kalivretenos A, Ghosh B, & Broedel SE (2012) Engineering a Hyper-catalytic Enzyme by Photoactivated Conformation Modulation. *Journal of Physical Chemistry Letters* 3(9):1142-1146.
47. Lin J, Prahlad J, & Wilson MA (2012) Conservation of oxidative protein stabilization in an insect homologue of parkinsonism-associated protein DJ-1. *Biochemistry* 51(18):3799-3807.
48. Kabsch W (2010) Integration, scaling, space-group assignment and post-refinement. *Acta crystallographica. Section D, Biological crystallography* 66(Pt 2):133-144.
49. Otwinowski Z & Minor W (1997) Processing of X-ray diffraction data collected in oscillation mode. *Macromolecular Crystallography, Pt A* 276:307-326.
50. Sierra RG*, et al.* (2016) Concentric-flow electrokinetic injector enables serial crystallography of ribosome and photosystem II. *Nature methods* 13(1):59-62.
51. Sauter NK, Hattne J, Grosse-Kunstleve RW, & Echols N (2013) New Python-based methods for data processing. *Acta crystallographica. Section D, Biological crystallography* 69(Pt 7):1274-1282.
52. Uervirojnangkoorn M*, et al.* (2015) Enabling X-ray free electron laser crystallography for challenging biological systems from a limited number of crystals. *eLife* 4.
53. Adams PD*, et al.* (2010) PHENIX: a comprehensive Python-based system for macromolecular structure solution. *Acta crystallographica. Section D, Biological crystallography* 66(Pt 2):213-221.
54. Emsley P & Cowtan K (2004) Coot: model-building tools for molecular graphics. *Acta crystallographica. Section D, Biological crystallography* 60(Pt 12 Pt 1):2126-2132.
55. Davis IW*, et al.* (2007) MolProbity: all-atom contacts and structure validation for proteins and nucleic acids. *Nucleic Acids Res* 35(Web Server issue):W375-383.
56. Wang J, Brudvig GW, Batista VS, & Moore PB (2017) On the relationship between cumulative correlation coefficients and the quality of crystallographic data sets. *Protein Sci* 26(12):2410-2416.
57. Wang J, Wang W, Kollman PA, & Case DA (2006) Automatic atom type and bond type perception in molecular mechanical calculations. *J Mol Graph Model* 25(2):247-260.
58. Eastman P & Pande VS (2015) OpenMM: A Hardware Independent Framework for Molecular Simulations. *Comput Sci Eng* 12(4):34-39.